IOP Publishing and International Atomic Energy Agency Nuclear Fusion
Nucl. Fusion **53** (2013) 113037 (13pp) doi:10.1088/0029-5515/53/11/113037

# Modelling debris and shrapnel generation in inertial confinement fusion experiments

**D.C. Eder[1], A.C. Fisher[1], A.E. Koniges[2] and N.D. Masters[1]**

[1] Lawrence Livermore National Laboratory, 7000 East Ave. Livermore, CA 94551, USA
[2] Lawrence Berkeley National Laboratory, 1 Cyclotron Road Berkeley, CA 94720, USA

E-mail: deder@llnl.gov

Received 12 March 2013, accepted for publication 4 September 2013
Published 24 October 2013
Online at stacks.iop.org/NF/53/113037

**Abstract**
Modelling and mitigation of damage are crucial for safe and economical operation of high-power laser facilities. Experiments at the National Ignition Facility use a variety of targets with a range of laser energies spanning more than two orders of magnitude (∼14 kJ to ∼1.9 MJ). Low-energy inertial confinement fusion experiments are used to study early-time x-ray load symmetry on the capsule, shock timing, and other physics issues. For these experiments, a significant portion of the target is not completely vaporized and late-time (hundreds of ns) simulations are required to study the generation of debris and shrapnel from these targets. Damage to optics and diagnostics from shrapnel is a major concern for low-energy experiments. We provide the first full-target simulations of entire cryogenic targets, including the Al thermal mechanical package and Si cooling rings. We use a 3D multi-physics multi-material hydrodynamics code, ALE-AMR, for these late-time simulations. The mass, velocity, and spatial distribution of shrapnel are calculated for three experiments with laser energies ranging from 14 to 250 kJ. We calculate damage risk to optics and diagnostics for these three experiments. For the lowest energy re-emit experiment, we provide a detailed analysis of the effects of shrapnel impacts on optics and diagnostics and compare with observations of damage sites.

## 1. Introduction

Understanding and modelling debris and shrapnel generation and associated damage effects on high-power laser systems is now possible through detailed 3D simulations. One goal of high-power laser systems is the demonstration of significant fusion yield based on inertial confinement of a capsule containing frozen hydrogen. The National Ignition Facility (NIF) at Lawrence Livermore National Laboratory (LLNL) has unique capabilities that support a wide range of inertial confinement fusion (ICF) experiments [1]. The quest for significant fusion yield on NIF is a large multi-laboratory effort [2]. In addition, ICF experiments are planned for the Laser MegaJoule (LMJ) facility under construction in France [3]. It is critical that experiments at NIF and LMJ have minimal debris/shrapnel related damage to optics and diagnostics. To assess and mitigate the damage risk to these components it is necessary to include the full-target structure and extend the simulations to late time (hundreds of ns). The ICF effort encompasses a wide range of campaigns to optimize target and laser parameters [4]. The majority of these targets are cryogenically cooled with a capsule located inside a high-$Z$ (Au or U) hohlraum liner having a wall thickness of ∼30 $\mu$m. The hohlraum liner is held by an outer Al structure referred to as the thermal mechanical package (TMP) having an average wall thickness of ∼300 $\mu$m [5]. Low-energy campaigns are used to study early-time x-ray load symmetry on the capsule, shock timing, and other physics issues. For some of these campaigns, there are changes to the target, e.g., adding a diagnostic hole in the hohlraum and TMP for x-ray imaging, or additional structures on the target, e.g., adding an Au cone directed at an optical interferometer for shock timing.

The ICF campaigns on NIF differ mainly in the type of capsule used, the potential addition of shock-timing cones and backlighting foils, and the laser parameters, e.g., energy, power, pointing, and wavelengths [6]. The re-emit campaign uses the lowest energy (∼14 kJ), which is less than 1% of the available laser energy [7]. For this campaign, a high-$Z$ Bi capsule is used and the symmetry of x-ray loading at the beginning of the ignition pulse is measured by imaging the x-rays re-emitted by this capsule. The images are obtained using image plates or a camera with a micro-channel plate (MCP) in front of a charge coupled device (CCD). Images are taken through the upper laser entrance hole (LEH) and through a viewing hole in the side of the target. The shock-timing campaign uses a range of laser energies spanning from approximately 140 kJ to more than 1 MJ depending on the number of shocks being studied [8]. The baseline ICF design on NIF has a total of four shocks passing through the capsule with the last one associated with the main laser pulse that contains the majority of the laser energy. In this paper, we focus on lower-energy (∼140 kJ) experiments that study the

 

first three shocks. We refer to this set of experiments as '1–3 shock-timing' experiments. To measure the timing of these three shocks as they pass through the capsule shell, an Au cone filled with liquid deuterium is inserted into the capsule and is pointed towards the velocity interferometer system for any reflector (VISAR), which is protected from shrapnel by a thick blast window [9]. The final low-energy experiment we discuss in this paper is part of the shock commissioning campaign with a laser energy of ∼250 kJ [10]. In this experiment a shock package is located at the wall of the hohlraum and an outer Au cone surrounds the package and points towards the VISAR. The outer Au cone is similar to the portion of the 1–3 shock-timing cone that lies outside the hohlraum but is not filled with liquid deuterium. We present late-time simulation results for each of these three campaigns and use the results to determine damage risk to optics and diagnostics.

Evaluating damage risk to NIF optics depends on details of the campaign and optical configuration. The wavelength of the amplified laser on NIF is in the infrared ($1\omega$) with approximately half the energy associated with an ignition pulse shape being converted into ultraviolet ($3\omega$) laser light in the final optics assembly (FOA). (Conversion efficiency is poor for the low-power portion of ignition pulses.) The remaining $1\omega$ light and some frequency doubled $2\omega$ light also enters the target chamber. However, NIF uses wedge focus lenses to shift the focal spots of the different wavelengths such that only $3\omega$ light enters the hohlraums. (In contrast, only $3\omega$ laser light enters the LMJ chamber.) The last optic in the FOA that the laser passes through prior to entering the NIF target chamber is a relatively thin piece of borofloat glass referred to as a disposable debris shield (DDS). The DDSs are roughly 7 m from the targets and are placed with a 2 m setback from the chamber wall. The NIF optics/beams are at angles of 23.5°, 30.0°, 44.5° and 50° as measured from the upper and lower poles of the target chamber. The set of beams at smaller angles are often referred to as inner beams as they strike the hohlraum wall further inside the target than the remaining beams, which are referred to as the outer beams. During the initial of operation of NIF, the DDSs were 1.1 mm thick but, after less than 1 year, the thickness was increased to 3.3 mm to reduce problems associated with gravitationally-induced bowing. For the target assessments discussed in this paper, the relevant DDS thickness is 3.3 mm. Located behind the DDSs are more expensive optics that would be damaged if shrapnel fragments penetrated the DDSs. Thus the determination of the probability of DDS penetration is an important component of all NIF target assessments. During NIF operation, penetrations and craters on DDSs are observed using a final optics damage inspection (FODI) system [11]. The number of optics inspected and the frequency of inspections depends on the calculated damage risk and the performance requirements of a given shot sequence. Observations of large craters indicate a higher risk of penetrations in subsequent similar shots. Up to ten DDSs are located in a cassette inside the FOA. Any of the ten DDSs can be inserted or re-inserted as needed, which allows a DDSs with lower transmission to be pulled for a shot requiring high transmission but later re-inserted for a different shot that has a lower transmission requirement. Thus accurate risk assessment can yield a significant cost saving benefit for the experimental campaign.

Evaluating damage risk to NIF diagnostics depends on what data is being obtained [6]. For example, the thickness of filters placed in front of an x-ray diagnostic depends on the energy of the x-rays being measured. This means that filters designed to allow transmission of soft x-rays are more likely to be penetrated by shrapnel because they are thinner. In addition to filters, there can be collimators and/or pinholes between the target and the diagnostic. These collimators/pinholes and the associated target configuration should be designed such that they are not penetrated by shrapnel fragments. Devices such as MCP-CCD cameras or image plates are generally located inside of a diagnostic instrument manipulator (DIM), which is inserted into the chamber. There are two DIMs located in the NIF chamber's equatorial plane and one polar DIM located at the top of the chamber. In contrast to optics, which are ∼7 m from the target, DIMs can be as close as ∼5 cm from the target. For re-emit experiments, there are pinhole arrays sandwiched between two collimators located in the nose cones of one equatorial DIM and the polar DIM. For shock-timing experiments, the VISAR diagnostic uses one of the equatorial DIMs.

In contrast with the work presented here, the vast majority of ICF simulations are on a timescale lasting only of order the duration of the driving pulse and do not consider structures outside the high-$Z$ hohlraum [12]. This type of simulation is not sufficient for modelling debris and shrapnel generation. Some work has been done extending hohlraum simulations out to late time to determine the spatial distribution of debris and x-ray loading [13, 14]. However, these simulations do not include details of the TMP, surrounding cooling rings, or ancillary structures such as cones. The addition of these components means that a given late-time simulation of a complex ICF target for debris and shrapnel generation must cover extreme variations in densities and temperatures ranging from low-density hot plasmas to cold fragmenting solids. The importance of understanding the risks associated with debris and shrapnel targets on NIF components is well established [15–17]. To evaluate these risks there has been significant effort applied to develop new numerical tools [18–23]. In addition, experiments have been conducted to study laser-induced fragmentation on various laser systems [24, 25]. Information from these experiments and the numerical capability that we developed is applied to model debris and shrapnel generation in ICF experiments discussed in this paper.

We first discuss the requirements for assessments associated with debris and shrapnel and our late-time simulations used to calculate the risk of damage to optics and diagnostics. We follow with simulation results in order of decreasing laser energy of 246, 146 and 14 kJ, for the shock commissioning, 1–3 shock-timing, and re-emit campaigns respectively. This was also the order that these campaigns were initially fielded on NIF. For the lowest energy re-emit campaign, we discuss in some detail the masses and velocities of shrapnel directed towards optics and diagnostics and the associated risk of damage to these components.

## 2. Assessments and late-time simulations

Large laser facilities such as NIF and LMJ are expensive to operate due, in part, to the large number and cost of optics

and diagnostics. To evaluate damage risk to these components associated with debris and shrapnel generation, details of the full target must be included in simulations. Important results of these simulations are the amounts of vaporized material, which is referred to as debris, and the amounts of solid and molten material, which is referred to as shrapnel. For low-energy experiments that are the focus of this paper, a significant fraction of the target is not vaporized. For both debris and shrapnel, the spatial distribution is important. Debris can deposit on optics and reduce their transmission by absorbing or scattering laser light. Loss of transmission can also be caused by debris-induced damage to the optics. In addition, the momentum associated with the rapidly expanding debris ('debris wind') can be of sufficient magnitude to damage and/or launch components close to the target. The deposited mass per unit area, which causes transmission loss, and the impulse loading per unit area decrease quadratically with distance. In contrast, shrapnel effects, e.g., penetration into an optic or diagnostic component, do not decrease with distance because of the relatively low-pressure vacuum (of order $10^{-6}$ Torr) in the NIF chamber. However, the number of such events per unit area decreases quadratically with distance.

The primary concern associated with shrapnel fragments (solid or molten) directed towards the NIF optics is penetration of the 3.3 mm thick DDSs. The penetration depth depends primarily on the velocity, mass, and density of the fragment. It also depends weakly on the material strength of a solid fragment or if the fragment is molten. We use an analytic formula for the critical velocity needed to penetrate a given thickness of glass. As we are looking for a conservative approximation for the penetration depth of shrapnel induced damage we will ignore the energy associated with crack initiation. Furthermore we assume that the damage will behave as a Hertzian cone fracture with the crack length, $c$, given by the following equation [26]:

$$c = \left(\frac{\chi_h P_{eff}}{K_{IC}}\right)^{2/3}, \tag{1}$$

where $\chi_h$ is a material constant, $K_{IC}$ is the fracture toughness for the material (we use $\chi_h = 0.048$ and $K_{IC} = 770\,000\,\mathrm{Pa}\sqrt{\mathrm{m}}$ for borosilicate glass), $P_{eff}$ is the effective maximum force of the contact [27]

$$P_{eff} = \left(\frac{5\pi\rho}{3}\right)^{3/5}\left(\frac{3k'}{4}\right)^{-2/5} v^{6/5} r^2, \tag{2}$$

where $\rho$, $r$ and $v$ are the density, radius and velocity of the projectile respectively, and

$$k' = \left(\frac{1-\nu_p^2}{E_p} + \frac{1-\nu_g^2}{E_g}\right), \tag{3}$$

where $E_p$, $\nu_p$ and $E_g$, $\nu_g$ are Young's moduli and Poisson's ratio, respectively, for the projectile and glass. We normally use steel properties for the projectiles $E_p = E_{steel} = 193 \times 10^9$ Pa and $\nu_p = \nu_{steel} = 0.3$ with glass parameters being $E_g = 62.75 \times 10^9$ Pa and $\nu_g = 0.2$. While steel is more dense than Al or Si, it is less dense than Au, so it an appropriate middle ground. The crack length going through the thickness, $t$, of the material is $c = t/\sin\theta$ and is minimum when the crack is orthogonal to the surface ($\theta = 90^\circ$)—and is therefore the same as the material thickness, i.e. yielding

$$t = \left(\frac{\chi_h P_{eff}}{K_{IC}}\right)^{2/3} \tag{4}$$

$$= \left(\frac{\chi_h}{K_{IC}}\left(\frac{5\pi\rho}{3}\right)^{3/5}\left(\frac{3k'}{4}\right)^{-2/5} v^{6/5} r^2\right)^{2/3} \tag{5}$$

we can then substitute the radius as a function of the fragment mass, $M$, $r = (3M/4\pi\rho)^{1/3}$ and then manipulate to give the critical velocity.

$$v_{crit}(t, M) = \left[\left(t^{3/2}\right)\left(\frac{K_{IC}}{\chi_h}\right)\left(\frac{4^{\frac{2}{3}}}{5^{\frac{3}{5}}}\right)\left(\frac{\pi\rho}{3}\right)^{\frac{1}{15}}\left(\frac{3k'}{4}\right)^{2/5}\right]^{\frac{5}{6}} M^{-\frac{5}{9}}. \tag{6}$$

This formula has been validated with experimental data using spherical steel projectiles impacting borofloat glass (see acknowledgments).

In the case of diagnostics, a primary concern is penetration of filters, collimators, and/or pinholes located between the target and expensive diagnostic components. The filters, collimators, and pinholes of interest are thin metal sheets. To calculate potential penetration we use formulas developed by Cour-Palais [28] in the form published by Christiansen [29]

$$d_c = \left[\frac{t_s}{k}\frac{HB^{0.25}\left(\rho_s/\rho_p\right)^{\frac{1}{2}}}{5.24\left(V\cos\theta/C\right)^{\frac{2}{3}}}\right]^{\frac{18}{19}} \quad \text{if } \left(\rho_p/\rho_s\right) < 1.5, \tag{7}$$

$$d_c = \left[\frac{t_s}{k}\frac{HB^{0.25}\left(\rho_s/\rho_p\right)^{\frac{3}{2}}}{5.24\left(V\cos\theta/C\right)^{\frac{2}{3}}}\right]^{\frac{18}{19}} \quad \text{if } \left(\rho_p/\rho_s\right) > 1.5, \tag{8}$$

where $d_c$ is the critical projectile diameter for the given velocity, $t_s$ is the shield thickness, $k = 3.0$, 2.2 and 1.8 for incipient spallation, detached spallation and perforation, respectively, HB is the Brinell hardness of the shield, $\rho_s$ and $\rho_p$ are the densities ($\mathrm{g\,cm^{-3}}$) of the shield and projectile, respectively, $V$ is the projectile velocity ($\mathrm{km\,s^{-1}}$), $\theta$ is the impact angle from target normal and $C$ is the sound speed in the shield material ($\mathrm{km\,s^{-1}}$). For potential penetration of Ta collimators discussed in the next section, we use $k = 2.2$, HB = 800, $\rho_s = 16.65\,\mathrm{g\,cm^{-3}}$ and $C = 3.4\,\mathrm{km\,s^{-1}}$.

The complex structures that we model combined with the need to calculate shrapnel sizes/masses requires 3D simulations. To address this need, a new 3D multi-physics multi-material code, ALE-AMR, was developed at LLNL in collaboration with researchers at Lawrence Berkeley National Laboratory (LBNL) and two University of California campuses in San Diego (UCSD) and Los Angeles (UCLA) [23]. The code has physics models that include arbitrary Lagrangian Eulerian (ALE) hydrodynamics, adaptive mesh refinement (AMR), thermal diffusion, radiation diffusion, laser/ion deposition, anisotropic material strength with material time history, and advanced models for fragmentation. Traditional ICF modelling codes, e.g., Hydra [30], Lasnex [31] and FCI2 [32], use ALE hydrodynamics, which is particularly beneficial

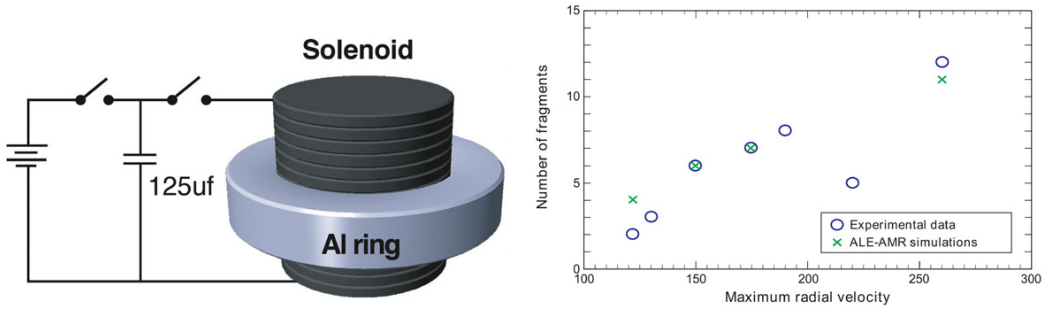


**Figure 1.** (Left) Schematic for the electromagnetically driven expanding ring experiments [33]. (Right) Comparison of data and simulation for the number of ring fragments as a function of maximum velocity of the ring.

for laser ablation and capsule implosion calculations, in contrast to doing Eulerian hydrodynamics on a stationary mesh. Codes using Eulerian hydrodynamics use AMR to accurately track shocks and other physical properties moving on the mesh. The approach of combining ALE hydrodynamics with AMR has a number of advantages including the ability to define the initial mesh accurately and during runtime to resolve features of interest. It is not practical to have all material boundaries conformal with zone boundaries for meshes associated with complex ICF targets. This means that there will be zones with multiple materials in the initial mesh. Additional mixed zones will be introduced during runtime as a result of remapping of the mesh as part of the ALE hydrodynamics. In order to accurately resolve the material boundaries of the target, we use the highest level of mesh refinement for all these mixed zones. We generally refine the mesh a factor of 3 in each dimension so one zone becomes 27 zones for one level of increased refinement in 3D simulations.

The open-source code ALE-AMR runs on various computational platforms at LLNL and at the National Energy Research Scientific Computing Center (NERSC) at LBNL. Experiments to study debris and shrapnel generation have been conducted at various smaller laser facilities to provide validation of our simulation capability [13, 23, 24]. The strength and failure models in the code have been benchmarked against the commercial code LS-DYNA and the ion deposition and hydrodynamic packages have been benchmarked against the LLNL code Hydra when it was first used to model heavy ion based inertial fusion energy experiments [34]. Researchers in France plan to use ALE-AMR to model LMJ targets in the future as that facility becomes operational. The code is also being considered for modelling material removal in magnetic fusion devices [35, 36]. Of particular relevance to the modelling discussed in this paper are our code validation efforts associated with cylindrically expanding Al structures, which have not been previously published. We compare simulations with fragmentation data for electromagnetically driven rings [33]. In the experiment, 1 mm thick Al rings with inner and outer diameters of 30.5 and 32.5 mm are placed around a solenoid, see left image in figure 1. A capacitor bank is charged to one of a variety of voltages and discharges 0.94–3.12 kJ of energy through the solenoid. The current flowing through the solenoid produces a large magnetic field, which in turn induces a current in the ring. This induced current resistively heats the ring with temperature increases ranging from 110 to 240 K. The current also results in a repulsive force between the solenoid and the ring, causing the ring to expand outward with maximum expansion velocities from 50 to 300 m s$^{-1}$. Finally, after each ring is accelerated, the fragments are collected, counted, and analysed. Our ALE-AMR ring simulations use a cylindrical mesh with a $5 \times 5$ element cross-section and 600 circumferential elements. We use Johnson–Cook strength and failure models for Al 6061-T6 parameters given in table 1. (These models and parameters are used in our NIF simulations discussed in the next section for the Al in the TMP surrounding the high-$Z$ hohlraums.) We use BdivK units: cm-g-$\mu$s-K, with energy units EU equivalent to Tergs. The Johnson–Cook $D_2$ parameter is varied from cell to cell with a uniform random distribution of $\pm 2.5\%$ in order to seed the rings with some structural variation. A radially oriented outward body force is applied to the to the ring over a Gaussian pulse in time centred at 28 $\mu$s with $\sigma = 7\,\mu$s. During a series of runs, the peak of this Gaussian is adjusted to produce various maximum ring velocities that matched the experimental data. The temperature of the ring is set to match the measured temperature corresponding to a given maximum velocity. Figure 1 shows good agreement between the experimental results and the ALE-AMR simulations.

**Table 1.** Aluminum 6061-T6 material parameters for Johnson–Cook models.

| Material parameter | Value (BdivK units) |
|---|---|
| Young's modulus | 0.68995 |
| Poisson's ratio | 0.32683 |
| Reference shear modulus | 0.26 |
| Bulk modulus | 0.664 |
| Density | 2.7 |
| Reference strain rate | 1.0 |
| Johnson–Cook A | 0.00324 |
| Johnson–Cook B | 0.00114 |
| Johnson–Cook C | 0.002 |
| Johnson–Cook n | 0.42 |
| Johnson–Cook m | 1.34 |
| Johnson–Cook $D_1$ | −0.77 |
| Johnson–Cook $D_2$ | 1.45 |
| Johnson–Cook $D_3$ | −0.47 |
| Johnson–Cook $D_4$ | 0.0 |
| Johnson–Cook $D_5$ | 1.6 |
| Room temperature | 294.0 |
| Melting temperature | 925.0 |

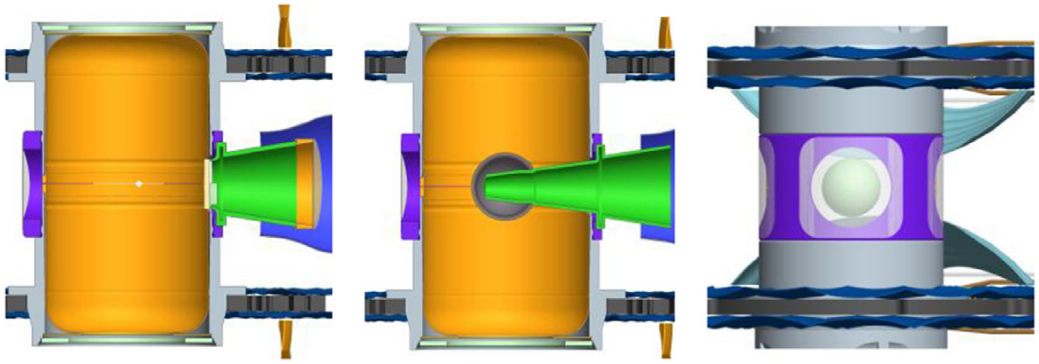

**Figure 2.** (Left) Shock commissioning target. (Centre) Shock 1–3 timing target. (Right) Re-emit target with Bi capsule.

## 3. Low-energy simulation results

Target drawings for the three campaigns discussed in this paper are shown in figure 2. On the left is the shock commissioning target with the Au hohlraum liner inside the Al TMP. The Si cooling rings sit against an Al TMP step with less of the ring shown on the left side. On either side of the cooling rings (shown as dark grey) are 35 $\mu$m thick waffled Al shields (shown as blue) to disperse the 1$\omega$ and 2$\omega$ light laser light that strikes the outside of ICF targets. The shock package is shown on the right side of the hohlraum wall with the Au cone (shown as green) attached to the TMP. An Al ring (shown as orange) is at the end of the Au cone. Surrounding the cone is a large cone shield (shown in blue) to block 1$\omega$ and 2$\omega$ light with only the part closest to the TMP shown. The cone is relatively thin with an Al layer placed between two plastic layers. The target for timing the first three shocks is shown in the centre image of figure 2. The Au cone passes through the hohlraum wall and the capsule shell. The capsule and the cone are filled with liquid deuterium. The re-emit target is shown as the right image of figure 2. The primary focus of the re-emit campaign is to measure the symmetry of the x-ray loading at the very start of the of the ignition pulse using a Bi capsule, which is seen through the an opening in the TMP diagnostic band (shown as purple) and the upper LEH. We discuss simulation results for each of these targets with laser energy 246, 146 and 14 kJ, for shock commissioning, 1–3 shock-timing, and re-emit campaigns, respectively.

Prior to discussing details of simulations for the three targets, we provide some background and general information. The cylindrical shape of ICF targets is a major benefit in reducing debris and shrapnel loading on the NIF optics that are located at angles between 23.5° and 50° from the upper and lower poles. The majority of debris and shrapnel from ICF targets is directed towards the poles or the waist of the NIF chamber because the response of loading on the inside surfaces of the target is to direct material 180° from the normal of the loading surface. Earlier simulations that focused on debris loading show a significant reduction of debris loading on optics as compared to isotropic distribution of debris [13]. For ICF targets that are shot at energies of order 1 MJ, the high-$Z$ hohlraum and the Al TMP are generally vaporized with portions of the Si cooling rings/supports and attached cones, if present, not vaporized. Silicon is used for cooling rings/supports not only because of its high thermal conductivity (significantly better than Al at cryogenic temperatures) but also for its brittle failure properties. Thus unvaporized Si is not expected to be a significant threat to NIF optics or diagnostics because the fragments are very small [19]. The curved property of the hohlraum wall, other than the portion directed towards the poles, results in a divergent velocity field as the target expands due to internal loading. This results in smaller fragments (both molten and solid) than what would be obtained from planar loading on flat targets. For all three experiments, we address potential damage risk to the NIF optics, i.e. the 192 3.3 mm thick DDSs. For the shock commissioning and 1–3 shock-timing experiments, the primary diagnostic is the VISAR, which is protected from shrapnel by a thick (~2.5 cm) blast window, and is not at risk for these experiments. Of course, the replacement rate for the blast window is a function of the debris/shrapnel loading on the optic. At the start of the experiments, there were sufficient spares to replace the blast window after every shot. For the re-emit experiment, the primary diagnostics are MCP-CCD cameras located in an equatorial plane DIM and in the polar DIM. In front of the cameras are two 500 $\mu$m thick Ta collimators located on either side of a 200 $\mu$m thick Ta pinhole array. Part of the assessment for this experiment is to determine if a Ta collimator is at risk to penetration by shrapnel from the target. We first discuss the relatively higher energy experiments, shock commissioning and 1–3 shock-timing, where we focus on the attached cones. We follow with results for the very low-energy re-emit experiment and focus on the unvaporized portions of the Al TMP.

For the shock commissioning and 1–3 shock-timing experiments we use a combination of 1D and 2D Hydra and Lasnex simulations to calculate laser deposition, hydrodynamics and radiation transport during the laser pulse. The calculated internal energy, kinetic energy, and total energy at the end of the laser pulse are given in table 2 for each of the two experiments. The difference between the total energy and the input laser energy is associated with radiation that has escaped the target. The rate that radiation energy continues to escape the target decreases as the target cools. Given that the late-time ALE-AMR simulations do not include this loss mechanism, we remove additional energy from the internal energy based on extrapolating the radiation loss rates. The modified internal energies, which are used as initial conditions

**Table 2.** Energy variables at end of laser pulse and start of ALE-AMR simulation.

| Energy variable | Shock com | Shock timing |
|---|---|---|
| Laser energy (kJ) | 246 | 146 |
| Kinetic energy (kJ) at end of laser pulse | 46.8 | 4.4 |
| Internal energy (kJ) at end of laser pulse | 133.1 | 79.6 |
| Total energy (kJ) at end of laser pulse | 179.9 | 84.0 |
| Modified internal energy (kJ) | 93.1 | 60.7 |
| Total energy (kJ) at start of ALE-AMR simulation | 139.9 | 65.1 |

for the late-time ALE-AMR simulations, are also given in the table. The kinetic energies are not modified.

The materials at the start of the ALE-AMR simulation of the shock commissioning experiment are shown in the upper left image (*a*) of figure 3 with 1/4 of the target shown. The simulation starts at the end of the 4 ns laser pulse with location, density, temperature of materials inside the hohlraum obtained from a combination of Hydra and Lasnex simulations. The gas fill (shown as green) is surrounded by the ablating Au hohlraum liner (shown as yellow). The shock package (shown as pink) is also ablated and moves into the hohlraum faster than the Au. The low-density gas fill that had already exited the target though the LEH is neglected. The Al TMP (shown as grey) is not heated at this time. The 500 $\mu$m thick Si cooling ring (shown as blue) with the slots and connecting tabs that contact the TMP are shown. There are 16 tabs on each ring. For simulations that include the Au cone, it is necessary to model 1/4 of the target as shown here. However, we have also run the shock commissioning and 1–3 shock-timing simulations using a 22.5° wedge (1/32 of the target) to focus on the dynamics of the TMP and cooling rings. The outer half of the shock package (shown as blue) and the Au cone (shown as yellow) with an Al ring (shown as grey) at the end of the cone are shown. The simulation at 220 ns is shown in the remaining images of figure 3. The density contours in the upper centre (*b*) and right (*c*) images show the plasma plume escaping out of the LEH and additional openings in the TMP. The Si cooling ring is still clearly visible. The lower left image (*d*) shows the entire mesh with patch boundaries showing the refinement level on a given patch. For running on large parallel machines, the distribution of patches to the available cores is implemented using the structured adaptive mesh refinement application infrastructure (SAMRAI) [37, 38]. For this simulation six levels of refinement are used, which roughly corresponds to a volume ratio of approximately $10^7$ to 1 for the largest to smallest zone. The centre lower image (*e*) in figure 3 shows the patch boundaries in the volume containing the target and plasma plume. The image on the bottom right (*f*) is an expanded view of the region shown in the centre images with three levels of mesh refinement seen in regions around Si cooling rings.

For this relatively high energy (246 kJ) shock commissioning experiment, the attached cone is of particular interest with regard to potential damage to the NIF optics. In order to have a clear view of the unvaporized cone at 215 ns, we show only material having a temperature below 3000 K and a density above 0.5 g cm$^{-3}$ in figure 4. The portion of the Au cone closest to the hohlraum/TMP has been vaporized and is thus not shown. The remaining cone is seen as high-density (yellow/green) material in the image. The lower density (blue) Al ring attached to the end of the Au cone is largely unvaporized but some of the outer portions have been vaporized by hot hohlraum material escaping out of the cone. The Si cooling ring is largely intact at this time and small portions of molten Al from the TMP are also visible. As discussed above, the brittle Si cooling rings are not considered a major treat to the optics, so we focus on the Au cone and Al ring. In figure 5 we show the initial profile of the Au cone (pale green) and Al ring (light blue) as well as lineouts of mass and velocities at 215 ns as a function of the axial position along the cone. The thickness of the cone is 100 $\mu$m with the Al having an average thickness of ~100 $\mu$m. The mass for material meeting the same temperature and density requirements as in figure 4 is shown per 100 $\mu$m of length. There is no material with axial location less than 3700 $\mu$m that meets this requirement as the cone closest to the hohlraum/TMP has been vaporized at this time. The increase in mass of the Au cone with axial location is associated with more material being unvaporized and with the increasing diameter of the cone. The drop in mass per 100 $\mu$m of length at 5700 $\mu$m is associated with the change from Au to lower density Al. The continued drop in mass is associated with the outer portions of the Al being vaporized. We also give the axial, radial (with respect to the cone axis), and total velocity of the Au cone and Al ring at 215 ns. The velocity is mainly radial except for the low-density Al region near end of cone where there is a significant axial component. The large radial velocities are associated with the hot hohlraum material escaping through the cone. The radial and total velocities of the solid Au are between 500 and 1500 m s$^{-1}$. The radial and total velocities of the solid Al are between 1500 and 2500 m s$^{-1}$. These velocities are no longer increasing at this time because the pressure driving the expansion has dramatically dropped as the hohlraum and TMP have largely vaporized. At these radial velocities, the Au and Al will break apart into fragments. While the integrated simulation shown here does not extend out to a time when this breaking would take place, we can estimate fragment size from earlier expanding ring simulations [19]. For these velocities we expect fragment sizes to be of order 100 $\mu$m. The mass of Au and Al fragments with dimension of 100 × 100 × 100 $\mu$m$^3$ is 19 and 2.7 × $10^{-3}$ mg, respectively. These masses combined with the range of expected velocities can be used in equation (1) or placed on figure 10, to determine potential penetration of DDSs. To evaluate potential penetration, we consider the top of the velocity range for Al and Au fragments. An Al fragment with a mass of 2.7 × $10^{-3}$ mg with a velocity of 2500 m s$^{-1}$, is calculated to be not quite capable of penetrating 1.1 mm thick DDSs. Therefore, the Al ring does not pose a penetration threat to the 3.1 mm thick DDSs used for this experiment. An Au fragment with a mass of 19 × $10^{-3}$ mg with a velocity of 1500 m s$^{-1}$, is calculated to be just able to penetrating 1.1 mm thick DDSs but not the 3.3 mm thick DDSs used in this experiment. Based on these calculations, no target material from the shock commissioning experiment is predicted to penetrate the NIF optics.

The cone used in the 1–3 shock-timing experiments is different from the shock commissioning experiment in that the

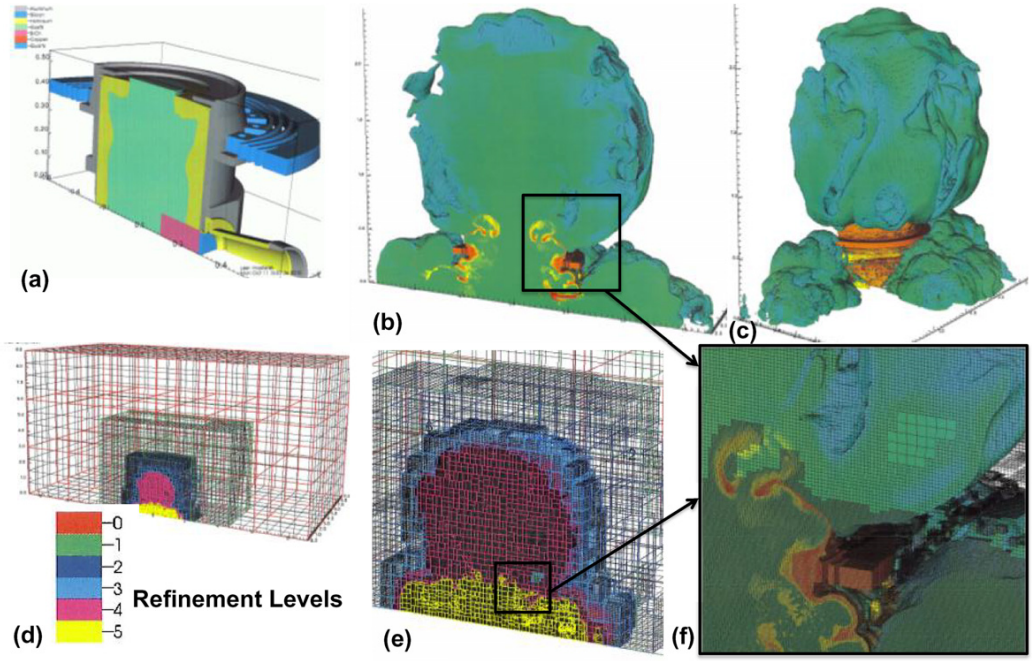


**Figure 3.** (*a*) Initial material specification at the start of ALE-AMR simulation. (*b*)–(*f*) Simulation at 220 ns. (*b*) Inside view showing plasma plume. (*c*) Outside view of plasma plume. (*d*) Entire mesh with patch boundaries showing the six levels of refinement. (*e*) Refinement levels and patch boundaries surrounding materials. (*f*) Expanded view of the region shown in (*b*) and (*e*) with three levels of mesh refinement seen in regions around Si cooling rings.

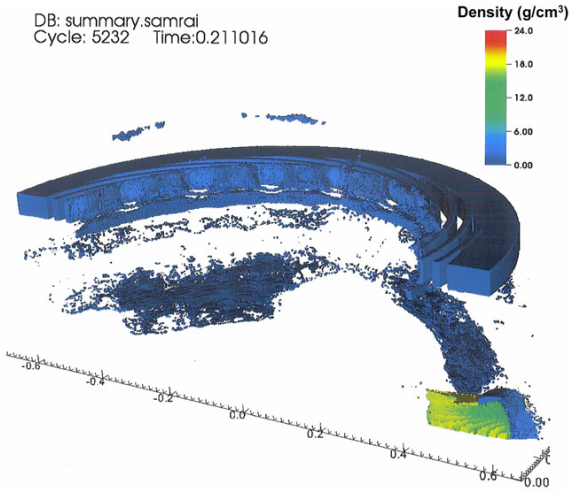


**Figure 4.** Shock commissioning simulation at 215 ns showing density on a linear scale. (The ALE-AMR simulation ran for 211 ns using conditions from a 4 ns simulation.) We show only material with temperature below 3000 K and density above 0.5 g cm$^{-3}$. The Si cooling rings and the Au/Al cone have not been vaporized.

cone extends into the hohlraum and the capsule. In addition the cone is filled with liquid deuterium in the 1–3 shock-timing experiments. To study the effect of fill, we show results of cone simulations with and without a deuterium fill. For these simulation we use initial conditions from Hydra simulations at the end of the laser pulse as already discussed for the shock commissioning experiment. We reduce the internal energy at the start of the ALE-AMR simulation as shown in the table to account for additional radiation losses. To study the effect of the fill, we model a portion of the full target using a 22.5° wedge with the axis along the axis of the cone with the hohlraum and TMP included in this wedge. In the left image of figure 6 we show the pressures at the start of the ALE-AMR simulation. In the right image of figure 6 we show the pressures 40 ns into the ALE-AMR simulation. We see that the hot hohlraum material has caused a portion of the inner cone to be indented towards the axis of the cone. In the left image of figure 7 we zoom in on this region and show the grid and material regions. In the right image of figure 7 we show this same region for a simulation at the same time without any deuterium fill. We see a relatively small effect of the cone being pushed somewhat closer to the cone axis. Simulations extended out to later times do not show any significant difference on cone dynamics associated with the presence or lack of deuterium fill. We find that the radial (as measured from the cone axis) expansion of the outer cone is much slower for the 1–3 shock-timing experiments as compared to the shock commissioning experiment. This is due in part to lower laser energy but also the inner cone prevents hot hohlraum material from escaping out through the outer cone. In general, the cone material is directed closer to the axis of the cone and does not pose a significant threat to the NIF optics. As already stated the VISAR diagnostic is protected by a thick blast window so the target does not pose a threat to this diagnostic. Both shock commissioning and 1–3 shock-timing experiments have been fielded on NIF with no penetrations of optics observed and no damage to the VISAR as predicted by simulations [39].

We now turn to the relatively low-energy re-emit experiment. The materials at the start of the ALE-AMR

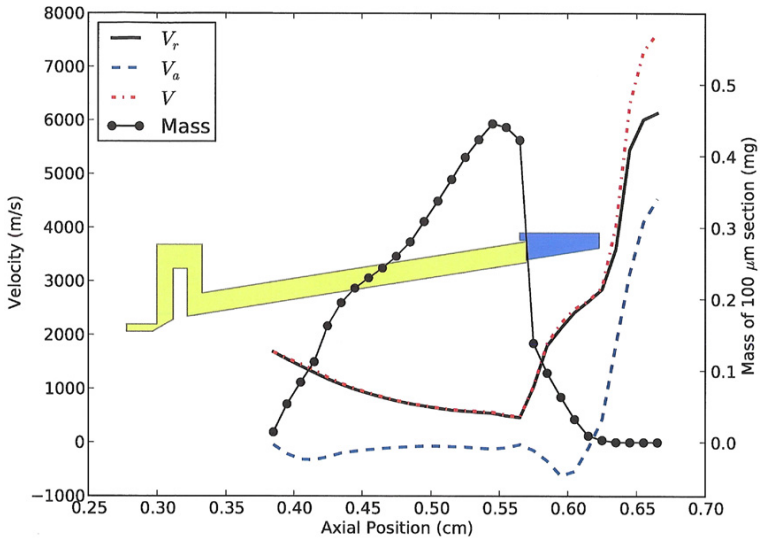


**Figure 5.** The initial cone geometry is shown as well as line outs at 215 ns of velocities and mass along the cone for the same temperature and density requirements as in figure 4. The mass of the cone is given in units of mg per 100 $\mu$m of length along the cone.

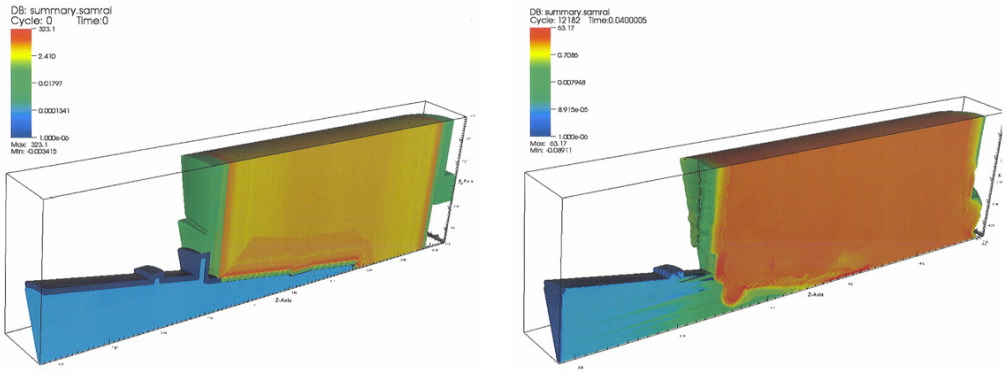


**Figure 6.** (Left) Three dimensional wedge simulation of hohlraum and keyhole cone showing pressure at the start of simulation. (Right) Pressure contours after 40 ns showing that the portions of the cone have pushed into the deuterium fill.

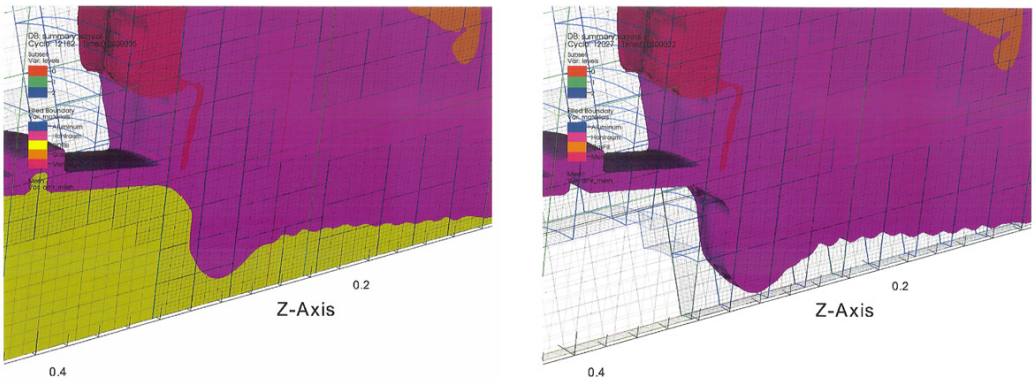


**Figure 7.** (Left) Zoom-in on a portion of the cone pushing into the deuterium fill with computational mesh shown. (Right) Simulation results showing the effect of removing the deuterium fill with vacuum.

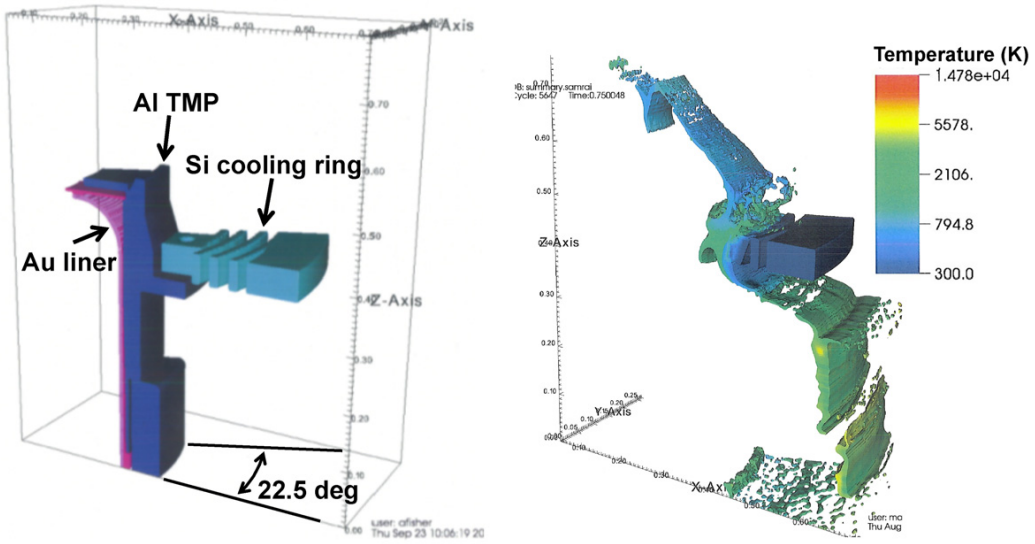


**Figure 8.** (Left) Initial geometry of simulated wedge showing target components. (Right) Simulation at 750 ns with temperature colour contours of all material with a density greater than 1 g cm$^{-3}$.

simulation for the 14 kJ re-emit experiment are shown on the left image in figure 8 for a 22.5° wedge simulation that models 1/32 of the entire target. This is in contrast to the wedge used to model the shock-timing cone above that modelled only a portion of the target. The image on the right gives the calculated temperature for all material with a density above 1 g cm$^{-3}$ at 750 ns. Approximately 1/3 of the total target mass is vaporized at this time. The Au hohlraum liner is completely vaporized. The majority of the Al is melted (Al melt temperature is 933.5 K) and the majority of the Si is solid. In order to determine the risk to optics and diagnostics associated with this experiment, we take into account the directionality of the expanding target components. In figure 9 we show only the material directed within 10° of the NIF optics. In other words all material directed between 13.5° and 60° from the pole. (The target is top-down symmetric and we are showing results associated with the upper pole.) As previously stated, we use Johnson–Cook strength and failure models for Al 6061-T6 with parameters given in table 1. Damage in an element is accumulated until it reaches a value of 1.0, at which point failure occurs. We consider zones that have reached the fracture point failed and insert a small fraction of void material into these failed zones negating their strength. These void fractions can grow and allow the material body to fragment. The damage state of the material is shown in figure 9 with red meaning the material has failed. We label the failed, molten and solid Al. In order to determine risk of penetration of DDSs by this collection of shrapnel fragments directed towards the optics, we must determine the mass and velocity of individual fragments. For individual solid fragments, we use the calculated masses and velocities. In addition there are collection of connected zones that have all reached the damage threshold. Such a global failure state for these zones indicates that we are not resolving the fragments sizes and we can bound the expected masses by using the masses of the individual zones in these volumes of failed material. The corresponding velocities of these fragments is just the zonal

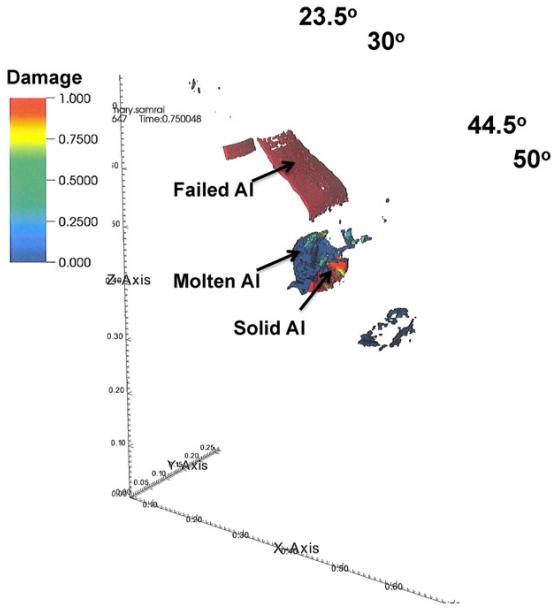


**Figure 9.** Simulation at 750 ns with damage colour contours of all material with a density greater than 1 g cm$^{-3}$ and directed within 10° of any optics. Direction of inner (23.5° and 30°) and outer (44.5° and 50°) optics is shown.

velocity. Finally, we consider molten material and the largest potential mass of individual droplets when the material reaches the optics. We use a very conservative bounding droplet size of 300 $\mu$m associated with the average thickness of the TMP. We use zonal velocities to calculate the average velocity for each droplet.

In figure 10 we show the penetration depths for all calculated fragments for the re-emit simulation at 750 ns that are directed towards the optics. The velocity of the fragments

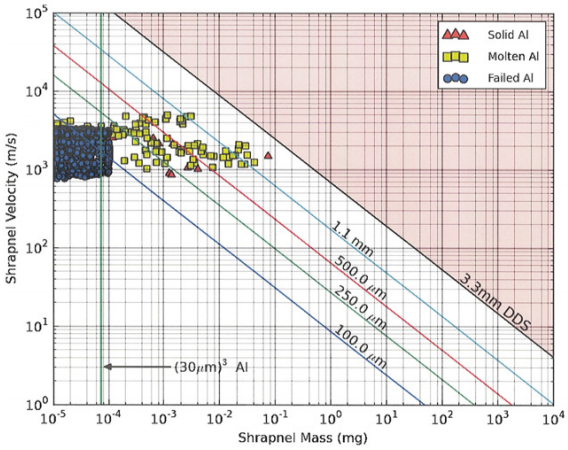


**Figure 10.** Mass and velocity of solid, molten, and failed Al shrapnel directed within 10° of NIF optics and penetration curves for different thicknesses of borofloat glass used for DDSs. Shaded region above the 3.3 mm DDS curve represents penetration of NIF DDSs.

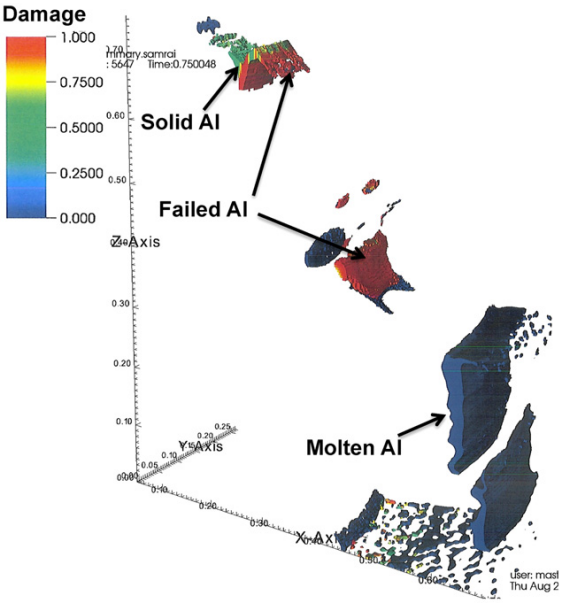


**Figure 11.** Simulation at 750 ns with damage colour contours of all material with a density greater than 1 g cm$^{-3}$ and directed within 10° of the polar or equatorial DIMs. Material labelled solid Al and nearby failed Al material are moving upward and are directed towards the polar DIM. The material labelled molten Al and the lower region of material labelled failed Al are moving to the right and are directed towards the equatorial DIM.

range from ∼700 to ∼5000 m s$^{-1}$. The most massive and most penetrating fragment is a solid piece of Al with a mass of ∼0.08 mg with a velocity ∼1500 m s$^{-1}$. This fragment is calculated to be able to penetrate the original DDS thickness of 1.1 mm but not the current thickness of 3.3 mm. There are approximately seven molten fragments that would also penetrate 1.1 mm but not the 3.3 mm thick DDSs. Each of the shrapnel fragments shown in the figure corresponds to 32 individual fragments because we are modelling only 1/32 of the entire target. However, the DDS optics occupy only ∼1/8 of the solid angle between 13.5° and 60° from each pole. Thus each fragment in the plot represents ∼4 impacts on the 192 DDSs. It is expected that the majority of the molten droplets would have smaller sizes than the bounding 300 $\mu$m size, which would result in a higher number of less penetrating impacts. The calculated penetration depths for the failed Al fragments is less than 250 $\mu$m and thus would not come close to penetrating even the original 1.1 mm thick DDSs. Inspection of the DDSs following the re-emit experiments did not find any penetrations of the DDSs, which is consistent with the simulation results [39].

We now consider the potential of damage to diagnostics for the re-emit experiments. The primary diagnostics are MCP-CCD cameras that are located in an equatorial plane DIM and in the polar DIM. They are use to image a high-$Z$ Bi capsule to determine the symmetry of x-ray loading at the beginning of the ignition pulse. Images are taken through the upper LEH and through a viewing hole in the side of the target. In front of the cameras are two 500 $\mu$m thick Ta collimators located on either side of a 200 $\mu$m thick pinhole array. The potential risk to the Ta collimator by shrapnel from the target must be determined. In figure 11 results of an ALE-AMR simulation at 750 ns are shown with damage colour contours of all material with a density greater than 1 g cm$^{-3}$ and directed within 10° of the polar or equatorial DIMs. We have excluded Si cooling ring material due to its brittle failure property as already discussed in the context of optical damage. All the Au material has vaporized, so only Al material from the TMP is a potential threat. Material labelled solid Al and nearby failed Al material are moving upward in the direction of the polar DIM. There is a relatively large mass of molten Al from the TMP that is moving outward from the waist of the target and a fraction of this material is expected to strike the equatorial DIMs. In addition there is some failed Al material that is also moving in the equatorial direction. The mass and velocity of fragments associated with solid, failed and molten Al are calculated in the same way as what was already discussed for evaluating damage to optics. The fragments that are directed within 10° of the polar DIM are shown in figure 12. Penetration curves for different thicknesses of Ta are given as well as a reference curve for a 3.33 mm thick DDS. The shaded region above the 500 $\mu$m Ta curve curve represents penetration of Ta collimator. In figure 13 a similar threat analysis image is given for shrapnel fragments directed towards the equatorial DIM.

Interpretation of results in figures 12 and 13 requires an understanding of how to unfold results from a narrow wedge simulation and information on the expansion properties of cylindrical-shaped targets. We model 1/16 of the top half of the target, which has top-bottom symmetry. There is a relatively small amount of radial (with respect to the hohlraum axis) expansion of the material directed towards the upper polar DIM. (Similar fragments would be directed to the lower pole but there are no relevant diagnostics in that direction.) This could result in fragments having an angular extent greater than what is simulated in the 22.5° wedge. In other words, an annular ring of material could break up into fewer than 16 fragments. However, these fragments would tend to strike the Ta collimators with the longer dimension parallel to the surface and the penetration depth would not be

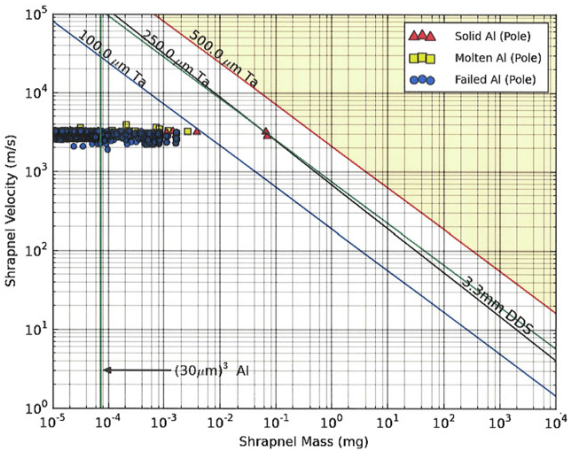


**Figure 12.** Mass and velocity of solid, molten, and failed Al shrapnel directed within 10° of polar DIM and penetration curves for different thicknesses of Ta and a 3.33 mm thick DDS for reference. Shaded region above the 500 $\mu$m Ta curve represents penetration of the Ta collimator.

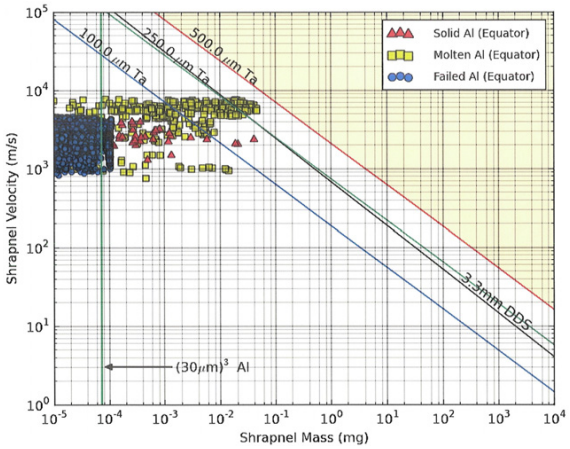


**Figure 13.** Mass and velocity of solid, molten, and failed Al shrapnel directed within 10° of equatorial DIM and penetration curves for different thicknesses of Ta and a 3.33 mm thick DDS for reference. Shaded region above the 500 $\mu$m Ta curve represents penetration of the Ta collimator.

significantly changed from what we calculate using masses and velocities from wedge simulations. In contrast, the large radial expansion associated with material directed towards the equatorial diagnostics means that for each fragment in the wedge simulation there are expected to be 32 similar fragments in the actual experiment. In other words, we do not expect any fragments to have an angular extent greater than the 22.5° associated with the wedge simulation angle. In figures 12 and 13 we give all fragments that are within 10° of the diagnostics but the actual diagnostics do not occupy the entire corresponding solid angles. The nose cones of the polar and equatorial DIMs are located 19 and 12.5 cm away from target centre, respectively. The diameter of the Ta collimators located in the front of the nose cones is 1.9 cm. This implies that the polar and equatorial collimators occupy ∼10% and ∼1% of the solid angles, respectively. These numbers give a lower limit to the expected number of impacts. The majority of fragments directed towards the polar DIM are confined in a cone less than 10°, which implies that a larger number of impacts is possible than that given using ratio of solid angles. This is also the case for the equatorial DIM.

Returning to the results shown in figure 12, we find that the vast majority of fragments both solid and molten do not have sufficient velocity/mass to penetrate a 100 $\mu$m thick Ta foil, which is 1/5 the thickness of the front Ta collimator in the polar DIM. There are two solid fragments with velocity/mass sufficient to penetrate a 250 $\mu$m thick Ta foil, which is 1/2 the thickness of the collimators. While these fragments would not penetrate the collimator, we would expect large damage sites associated with impact. We also see that these fragments, if directed towards the optics, have the potential to penetrate a 3.3 mm thick DDS. The actual number of impacts on the polar collimator associated with these two fragments depends on how the fragments breakup in the angular dimension not resolved by the narrow wedge simulation and how directed they are towards the polar axis as discussed above. In general, we expect of order 1–10 fragments to impact the polar collimator. In the left image of figure 14 we show damage sites on the nose cone and collimator of the polar DIM following a single re-emit experiment. The collimator was not penetrated, which is consistent with simulations, and the five large damage sites are circled. Note that all sites appear to be created by fragments that are curved and have an extent that is longer in a dimension parallel to the surface. These impacts are consistent with fragments have an angular extent greater than 22.5° associated with the wedge simulation as discussed above. Two other polar nose cones that were inspected following a single re-emit experiment showed single large impact sites [39].

The corresponding results for the equatorial DIM are shown in figure 13. We see that if the molten Al droplets have the very conservative mass associated with droplets with a bounding droplet size of order 300 $\mu$m, we would not expect any penetration by molten droplets but the potential of large damage sites. In addition there are three solid fragments with the ability to penetrate between 100 and 250 $\mu$m that would also produce large damage sites but again no penetration of the 500 $\mu$m thick front collimator. As discussed above each fragment in figure 13 is associated with 32 fragments in the experiment. However, the collimator occupies only 1% of the solid angle corresponding to the band ±10° above and below the DIM. Thus on average 3 fragments in figure 13 would correspond to 1 expected damage site on the equatorial collimator. This number is expected to be somewhat large as most material is directed at angles less than 10°. In the right image of figure 14 we show damage sites on the nose cone and collimator of the equatorial DIM following a single re-emit experiment. Two large and one somewhat smaller damage sites are circled. Two other equatorial nose cones that were inspected following a single re-emit experiment showed either two or three large impact sites [39], with no penetration of the collimator. Based on these results it appears that the impact sites are likely due to the solid fragments that were calculated to be directed towards the diagnostics and that the molten material breaks up into droplets that are too small to produce large damage sites. Analysis of the 200 $\mu$m thick Ta pinhole

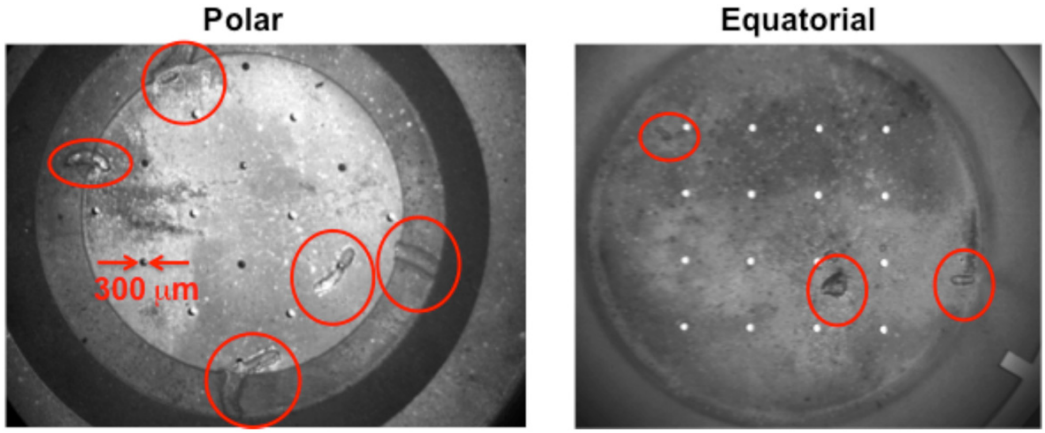


**Figure 14.** Damage sites on the collimators and nose cones of the polar and equatorial DIMs following a re-emit experiment are shown. The Ta collimators have sixteen 300 $\mu$m diameter holes facing the target. Large damage sites are circled.

arrays located behind the front collimators, show no evidence of penetration either. The area of the pinhole array that is exposed to shrapnel is limited to be just the area associated with the sixteen 300 $\mu$m diameter holes.

## 4. Conclusions

We show results for full-target simulations for three different low-energy ICF experiments fielded at the NIF and the associated damage risk to optics and diagnostics. These experiments are used to study early-time x-ray load symmetry on the capsule, shock timing, and other physics issues. For the shock commissioning and 1-3 shock-timing experiments, the hohlraum and TMP are largely vaporized and the outer Au/Al cone is of primary interest. This cone can have a significant radial velocity with respect to the cone axis and solid fragments are a potential threat to NIF optics. However, we show that for the calculated masses and velocities of shrapnel are not sufficient to result in penetrate of the 3.33 mm thick DDSs used to protect the expensive NIF optics. This result has been confirmed by analysis of the DDSs following a a number of these experiments with no penetrations observed. The primary diagnostics for these experiments is the VISAR, which is protected by a sufficiently thick blast window. For the 1–3 shock-timing experiment, we show that the use of liquid deuterium fill did not have a significant effect on cone dynamics. For the lowest energy re-emit experiment, a significant fraction of the Al TMP is not vaporized and is a potential threat to both optics and diagnostics. Based on results of a wedge simulation, we show that the 3.33 mm thick DDSs should not be penetrated by target shrapnel, which is consistent with observations of no penetration. We also calculate damage risk to diagnostics and determine that the fragments should not penetrate the 500 $\mu$m thick front collimator. However, large impact sites are expected on both polar and equatorial nose cones and collimators as confirmed by observations. These calculations are done using a 3D multi-physics multi-material hydrodynamics code, ALE-AMR, with input conditions from other ICF codes for two of the experiments. We are in the process of testing surface tension models in ALE-AMR, which can be used to predict droplet sizes of molten material. For these experiments the major threat to optics and diagnostics is associated with solid fragments. It appears that the choice of Si for the cooling rings and supports is appropriate as there is no evidence of DDS penetration by material from the cooling rings and support for these or other ICF experiments at the NIF.

We have shown that full-target simulations of ICF targets cover extreme ranges in densities and temperatures spanning from low-density hot plasmas to cold fragmenting solids. New numerical capabilities, as shown in this paper using the ALE-AMR code, allow one to determine the generation of debris/shrapnel and evaluate the damage risk to optics and diagnostics. While these simulations must be done in 3D, we have shown that critical results can be obtain by modelling as little as 1/32 of the entire target. For targets with less symmetry, we show that modelling 1/4 of the target is sufficient. In addition to ICF experiments, we have also modelled a wide range of other experiments on NIF to determine the damage risk associated with debris and shrapnel. In some cases, significant redesign of the experiment based on ALE-AMR simulations is required to minimize risk of damage [40]. As NIF transitions into a user facility and with the start of experiments at LMJ, there will be continued need for complex full-target simulations of proposed experiments.

## Acknowledgments

We thank NIF management, in particular, Drs Brian MacGowan and Otto Landen, for support and encouragement of this project. We acknowledge many useful conversations with Dr David Bailey on numerical and modelling issues. Professor David Benson at UCSD provided valuable insight on computational modelling of fragmentation. Dr Tayyab Suratwala developed the formula used to calculate penetration depths in glass and Dr Mike Tobin conducted experiments that validated this formula. Drs Harry Robey, David Braun, and Jose Milovich provided results from early-time ICF simulations that were used as inputs for some of the simulations. Dr Rahul Prasad measured impacts sites observed on collimators and DIM nose cones. The work performed by LLNL is under the auspices of the US Department of Energy

under Contract DE-AC52-07NA27344. The work performed by LBNL is supported by the Office of Science, US Department of Energy under Contract DE-AC02-05CH11231. Code development research used resources of the National Energy Research Scientific Computing Center, which is supported by the Office of Science of the US Department of Energy under Contract No DE-AC02-05CH11231. IM#:LLNL-JRNL-626315.

## References

[1] Moses E.I. 2010 *J. Phys.: Conf. Ser.* **244** 012006
[2] Lindl J.D. *et al* 2011 *Nucl. Fusion* **51** 094024
[3] Lion C. 2010 *J. Phys.: Conf. Ser.* **244** 012003
[4] Edwards M.J. *et al* 2011 *Phys. Plasmas* **18** 051003
[5] Atherton L.J. *et al* 2008 *J. Phys.: Conf. Ser.* **112** 032063
[6] Landen O.L. *et al* 2011 *Phys. Plasmas* **18** 051002
[7] Dewald E.L. *et al* 2011 *Phys. Plasmas* **18** 092703
[8] Robey H.F. *et al* 2011 *Phys. Plasmas* **19** 042706
[9] Celliers P.M., Bradley D.K., Collins G.W., Hicks D.G., Boehly T.R. and Armstrong W.J. 2004 *Rev. Sci. Instrum.* **75** 4916
[10] Boehly T.R. *et al* 2009 *Phys. Plasmas* **16** 056302
[11] Conder A., Alger T., Azevedo S., Chang J., Glenn S., Kegelmeyer L., Liebman J., Spaeth M. and Whitman P. 2008 *SPIE Proc.* **6720** 10
[12] Meezan N.B. *et al* 2010 *Phys. Plasmas* **17** 056304
[13] Eder D., Koniges A., Jones O., Marinak M., Tobin M. and MacGowan B. 2004 *Nucl. Fusion* **44** 709–19
[14] Koniges A.E., Marinak M.M. and Tipton R. 2004 *Inertial Fusion Sciences and Applications: State of the Art 2003 (Monterey, CA, USA)* (American Nuclear Society) p 261
[15] Eder D. *et al* 2006 *J. Physique IV* **133** 721
[16] Eder D., Koniges A., Landen O., Masters N., Fisher A., Jones O., Suratwala T. and Suter L. 2008 *J. Phys.: Conf. Ser.* **112** 032023
[17] Eder D.C. *et al* 2010 *J. Phys.: Conf. Ser.* **244** 032018
[18] Koniges A.E., Anderson R.W., Wang P., Gunney B.T.N., Becker R., Eder D.C. and MacGowan B.J. 2006 *J. Physique IV* **133** 587
[19] Fisher A., Masters N., Dixit P., Benson D., Koniges A., Anderson R., Gunney B., Wang P. and Becker R. 2008 *J. Phys.: Conf. Ser.* **112** 022027
[20] Masters N.D., Anderson R., Elliot N., Fisher A., Gunney B. and Koniges A. 2008 *J. Phys.: Conf. Ser.* **112** 022017
[21] Fisher A., Bailey D., Kaiser T., Gunney B., Masters N., Koniges A., Eder D. and Anderson R. 2010 *J. Phys.: Conf. Ser.* **244** 022075
[22] Masters N.D., Kaiser T.B., Anderson R.W., Eder D.C., Fisher A.C. and Koniges A.E. 2010 *J. Phys.: Conf. Ser.* **244** 032022
[23] Koniges A.E. *et al* 2010 *J. Phys.: Conf. Ser.* **244** 032019
[24] Koniges A. *et al* 2008 *J. Phys.: Conf. Ser.* **112** 032072
[25] Meyers M.A. *et al* 2009 *Proc. DYMAT (Brussels, Belgium)* (EDP Sciences) p 999 www.dymat-proceedings.org
[26] Lawn B. 1993 *Fracture of Brittle Solids* (Cambridge: Cambridge University Press)
[27] Knight C.G., Swain M.V. and Chaudhri M.M. 1977 *J. Mater. Sci.* **12** 1573–86
[28] Cour-Palais B.G. 1987 *Int. J. Impact Eng.* **5** 221
[29] Christiansen E.L. 1993 *Int. J. Impact Eng.* **14** 145
[30] Marinak M.M., Haan S.W., Dittrich T.R., Tipton R.E. and Zimmerman G.B. 1998 *Phys. Plasmas* **5** 1125
[31] Zimmerman G.B. and Kruer W.L. 1975 *Comment. Plasma Phys. Control. Fusion* **2** 51
[32] Holstein P.A. *et al* 2004 *Nucl. Fusion* **44** S177–84
[33] Altynova M., Hu X. and Daehn G.S. 1996 *Metall. Mater. Trans.* A **27** 1837
[34] Koniges A.E. *et al* 2013 *J. Phys.: Conf. Ser.* at press
[35] Koniges A.E., Eder D.E., Wan A.S., Scott H.A., Dalhed H.E., Mayle R.W. and Post D.E. 1997 *J. Nucl. Mater.* **241–243** 244
[36] Mioduszewski P.K., Owen L.W., Spong D.A., Fenstermacher M.E., Koniges A.E., Rognlien T.D. and Umansky M.V. 2007 *Fusion Sci. Technol.* **51** 238
[37] Hornung R.D. and Kohn S.R. 2002 *Concurrency Comput.: Practice Experience* **14** 347–68
[38] Gunney B., Wissink A.M. and Hysom D.A. 2006 *J. Parallel Distributed Comput.* **66** 1419–30
[39] Eder D.C. *et al* 2013 *J. Phys.: Conf. Ser.* at press
[40] Fournier K.B. *et al* 2010 *Rev. Sci. Instrum.* **81** 075113